Nano Research 2015, 8(11): 3651–3661
DOI 10.1007/s12274-015-0865-0
Research Article
ISSN 1998-0124
CN 11-5974/O4

Interlayer interactions in anisotropic atomically thin rhenium diselenide

Huan Zhao[1,§], Jiangbin Wu[2,§], Hongxia Zhong[3,5], Qiushi Guo[4], Xiaomu Wang[4], Fengnian Xia[4], Li Yang[3], Pingheng Tan[2] (✉), and Han Wang[1] (✉)

[1] *Ming Hsieh Department of Electrical Engineering, University of Southern California, Los Angeles, CA 90089, USA*
[2] *State Key Laboratory of Superlattices and Microstructures, Institute of Semiconductors, Chinese Academy of Sciences, Beijing 100083, China*
[3] *Department of Physics, Washington University in St Louis, St Louis, MO 63130, USA*
[4] *Department of Electrical Engineering, Yale University, New Haven, CT 06511, USA*
[5] *State Key Laboratory for Mesoscopic Physics and Department of Physics, Peking University, Beijing 100871, China*
[§] *These authors contributed equally to this work.*

Received: 28 April 2015
Revised: 16 July 2015
Accepted: 22 July 2015

KEYWORDS
rhenium diselenide, Raman, photoluminescence, anisotropy

ABSTRACT

In this work, we study the interlayer phonon vibration modes, the layer-number-dependent optical bandgap, and the anisotropic photoluminescence (PL) spectra of atomically thin rhenium diselenide ($ReSe_2$) for the first time. The ultralow frequency interlayer Raman spectra and the polarization-resolved high frequency Raman spectra in $ReSe_2$ allow the identification of its layer number and crystal orientation. Furthermore, PL measurements show the anisotropic optical emission intensity of the material with its bandgap increasing from 1.26 eV in the bulk to 1.32 eV in the monolayer. The study of the layer-number dependence of the Raman modes and the PL spectra reveals relatively weak van der Waal's interaction and two-dimensional (2D) quantum confinement in the atomically thin $ReSe_2$. The experimental observation of the intriguing anisotropic interlayer interaction and tunable optical transition in monolayer and multilayer $ReSe_2$ establishes the foundation for further exploration of this material in the development of anisotropic optoelectronic devices functioning in the near-infrared spectrum, which is important for many applications in optical communication and infrared sensing.

1 Introduction

Over the past few years, the transition metal dichalcogenide (TMDC) family [1–6] of two-dimensional (2D) materials have attracted considerable interest among physicists, chemists, engineers, and material scientists because of their unique physical and chemical properties resulting from 2D quantum confinements,

Address correspondence to Han Wang, han.wang.4@usc.edu; Pingheng Tan, phtan@semi.ac.cn

unique lattice structures, and interlayer coupling (or the absence of it in their monolayer (1L) form). Recently, 2D materials with strong in-plane anisotropic properties, such as black phosphorus [7–11], have been proposed for developing new devices with promising applications in electronics [12, 13], optoelectronics [14–18], and thermoelectrics [19]. However, the selection of 2D materials with strong in-plane anisotropy has been very limited, and only a few studies have been devoted to transition metal dichalcogenide materials with strong in-plane anisotropy. Therefore, their anisotropic optical and phonon properties and the anisotropy in their interlayer interactions have not yet been fully revealed.

In this work, we study the anisotropic interlayer interactions in an important TMDC 2D material with reduced symmetry—atomically thin rhenium diselenide ($ReSe_2$)—by investigating its interlayer phonon vibration modes, the layer-number dependent optical bandgap, and the anisotropic photoluminescence (PL) spectra for the first time. The ultralow frequency interlayer Raman spectra combined with the high frequency Raman measurements allow deterministic identification of the $ReSe_2$ layer number and crystal orientation. The PL measurements show that the anisotropic optical emission intensity, which depends on the polarization of the incoming light with the bandgap, increases from 1.26 eV in the bulk to 1.32 eV in the monolayer. This is consistent with theoretical results based on first-principle calculations using density functional theory (DFT). A systematic study of the polarization-resolved high frequency Raman spectra in monolayer and bilayer (2L) $ReSe_2$ is also carried out for the first time. Study of the layer-number dependence in the high frequency Raman modes and PL indicates relatively weak van der Waal's (vdW) interaction and 2D quantum confinement in atomically thin $ReSe_2$. The results reveal the intriguing interlayer interaction and anisotropic optical transition in monolayer and multilayer $ReSe_2$, which offers potential for developing anisotropic optoelectronic devices functioning in the near-infrared (NIR) spectrum.

$ReSe_2$ is a layered transition metal dichalcogenide with vdW interaction between layers. As shown in Fig. 1(a), every unit cell of monolayer $ReSe_2$ contains four formula units, which includes two categories of

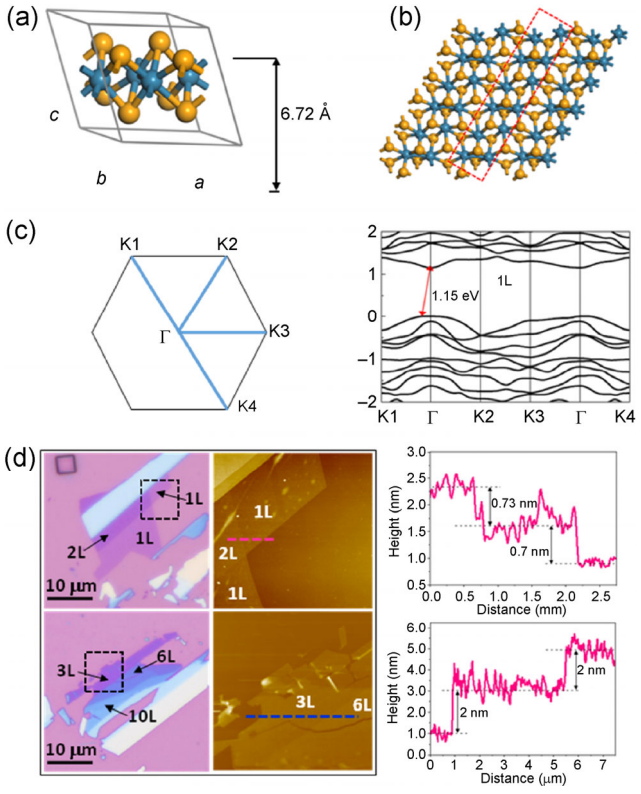

Figure 1 (a) Top: the unit cell of $ReSe_2$ crystal. ***a***, ***b***, and ***c*** are the three lattice vectors. Re and Se atoms are colored blue and yellow, respectively. Bottom: the top view of $ReSe_2$ crystal. The clustering of Re atoms forms the Re chains along the lattice vector ***a*** direction, as shown in the red-dotted-line box. (b) The calculated bandstructure of $ReSe_2$ monolayer. K paths are shown in the Brillouin zone above. The arrow indicates the transition from the top of the valence band to the bottom of the conduction band. Fermi level has been set to zero. (c) Left side: the optical and AFM image of monolayer and few-layer $ReSe_2$. Right panel: the AFM height data measured along the pink and blue dotted lines shown on the left.

Re atoms together with four categories of Se atoms. The Se atoms on top and bottom sandwich the Re atoms in the middle to form a monolayer lattice of $ReSe_2$. Unlike common TMDCs such as MoS_2 and WSe_2, which crystallize in the hexagonal (H) phases, $ReSe_2$ crystals exhibit a distorted $CdCl_2$-type lattice structure [20]. Owing to Peierls distortion [21], adjacent Re atoms are bonded in the form of zigzag four-atom clusters [22], which align along the direction of the lattice vector ***a*** to form Re chains (see Fig. 1(b)). Calculations have revealed that such a distorted octahedral (1T) crystal structure has lower energy than its hexagonal counterpart, and is thus more stable [23]. This clustering of Re atoms has also been

discovered in ReS_2 crystals [20, 24], contributing to distortion of the lattice geometry and stabilization of the crystals. Owing to its distorted 1T nature, $ReSe_2$ has strong in-plane anisotropy in its optical [25–27] and electronic [28–32] properties. Figure 1(c) shows the Brillouin zone of the monolayer $ReSe_2$, which is hexagonal with unequal side lengths. The band structure of monolayer $ReSe_2$ predicted by first-principle calculations is also shown in Fig. 1(c). The Perdew–Burke–Ernzerhof (PBE) exchange-correlation function under general gradient approximations (GGA) was applied in the calculations. Spin–orbit coupling (SOC) was taken into account, and ultrasoft pseudopotential was applied. The calculated bandgap is 1.15 eV. It is well known that GGA tends to underestimate the bandgap of 2D materials [33], so the actual intrinsic bandgap is likely to be larger than 1.15 eV, as confirmed by our experimental results that are discussed later. As seen in the energy band diagram, the bottom of the conduction band is located at the Γ point, while the top of the valence band is located near the Γ point, indicating that monolayer $ReSe_2$ is an indirect bandgap semiconductor.

2 Experiments and results

To investigate the interlayer interactions in this 2D material with reduced symmetry, $ReSe_2$ flakes were prepared on Si/SiO_2 substrates by the standard micromechanical exfoliation method [34]. Monolayer and few-layer samples were first located by optical contrast using an optical microscope, and then, the layer numbers were verified based on the height information measured by atomic force microscopy (AFM). Figure 1(d) shows the optical micrograph and the AFM data for monolayer and few-layer $ReSe_2$ flakes. According to the AFM morphology, the thickness of monolayer $ReSe_2$ is about 0.7 nm, which is in agreement with the interlayer distance obtained by powder diffraction [35]. $ReSe_2$ samples in their monolayer and few-layer forms are robust in air and show no clear signs of degradation after several months in an ambient environment.

The interlayer shear (C) and layer-breathing (LB) Raman modes of a layered material directly reflect its interlayer vdW coupling [36–42]. These modes only occur in multilayer $ReSe_2$, but not in the monolayer samples. As shown in Fig. 2(a), the C and LB modes often occur in the ultralow frequency region (< 50 cm^{-1}) of the Raman spectra in TDMCs because the vdW coupling is a much weaker interaction compared to the intralayer modes where the lattice atoms interact through the much stronger atomic bonding. In general, there are N–1 pairs of C modes and N–1 LB modes in an N-layer 2D layered material. For in-plane isotropic materials, such as graphene [36] and MoS_2 [37], each pair of C modes is doubly degenerate and have the same frequency. For an in-plane anisotropic 2D material of $ReSe_2$, each pair of C modes is not degenerate in principle, which means that there are 2(N–1) C modes with different frequencies in an N-layer sample and these 2(N–1) C modes can be divided into two categories based on the vibration directions. Although $ReSe_2$ is an

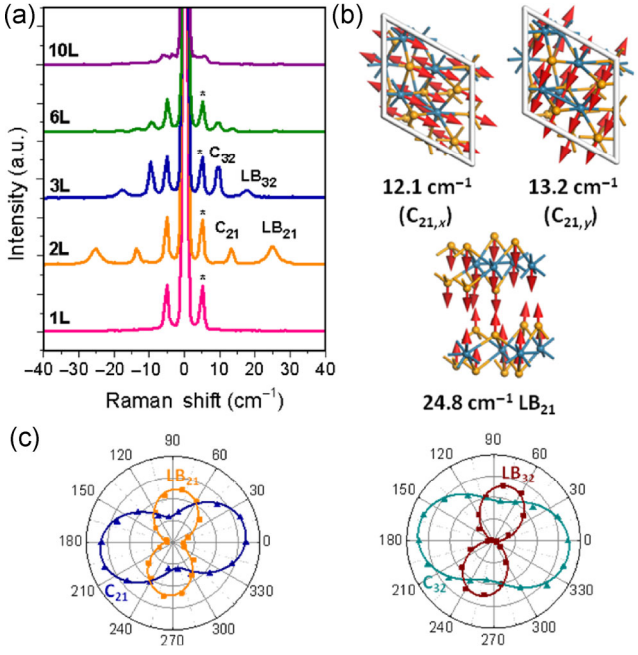

Figure 2 (a) Interlayer Raman modes in monolayer and few-layer $ReSe_2$. C and LB denote shear and breathing modes. Note that the two peaks around 5 cm^{-1} marked by stars are not Raman signals. They are due to Brillouin scatterings of silicon. (b) Schematic of the three low frequency phonon vibration modes of bilayer $ReSe_2$ obtained from first-principle calculations. From left to right, they correspond to the two shear modes located at 12.1 and 13.2 cm^{-1}, and one breathing mode located at 24.8 cm^{-1}. (c) Polarization-resolved Raman peak intensity of bilayer (left panel) and trilayer (right panel) $ReSe_2$. The intensity of each peak has been normalized with respect to the intensity of the Si peak. The dots in both figures represent experimental data, while the lines in both figures are theoretical fits from the Raman tensor analysis.

anisotropic material, the lattice constants of directions *a* (6.7 Å) and *b* (6.6 Å) are almost equal, which suggests that each pair of C modes of the material tend to overlap together because of their small frequency separation. First principle calculations using DFT (Fig. 2(b)) predict two C modes at 12.1 and 13.2 cm^{-1}, respectively, and a LB mode at 24.8 cm^{-1}. Figure 2(a) exhibits the ultralow frequency modes in monolayer, bilayer, trilayer (3L), six-layer (6L), and ten-layer (10L) $ReSe_2$. The spectrum for bilayer $ReSe_2$ has the C mode at 13.5 cm^{-1} and the breathing mode at 25.0 cm^{-1}. Since the theoretical difference between the two C modes in frequency are as small as 1 cm^{-1}, the peak measured at 13.5 cm^{-1} for bilayer $ReSe_2$ should correspond to the overlap of the two calculated C modes at 12.1 and 13.2 cm^{-1}. The experimental overlap is determined by fitting the C_{21} modes with two peaks, as shown in Fig. S3 in the Electronic Supplementary Material (ESM). Figure 2(b) shows the lattice vibration displacement directions for the three modes. The C and LB modes predicted by DFT calculations for trilayer $ReSe_2$ are included in Fig. S4 in the ESM.

Given an *N*-layer $ReSe_2$, we use C_{NN-i} and LB_{NN-i} (i = 1, 2, ⋯, N–1) to denote the N–1 C modes and N–1 LB modes. Here, C_{N1} and LB_{N1} (i.e., $i = N$–1) are the highest frequency C and LB modes, respectively. As shown in Fig. 2(a), no peaks corresponding to interlayer Raman modes are detected in the monolayer sample. The C_{21} and LB_{21} modes are observed at 13.5 and 25.0 cm^{-1} in the bilayer flake, respectively. However, only C_{32} (9.5 cm^{-1}) and LB_{32} (17.7 cm^{-1}) are detected in trilayer $ReSe_2$. The C_{31} and LB_{31} modes are silent.

Moreover, not all C and LB modes are observed in the six-layer and ten-layer samples. The likely reason for the absence of other C and LB modes is their much weaker electron phonon coupling compared to the lowest frequency modes, which is similar to the case of the highest frequency C modes in multilayer graphene [36]. The frequencies of all the C and LB modes in six-layer and ten-layer $ReSe_2$ are listed in Table S1 in the ESM. Moreover, the intensities of the low-frequency modes decrease with increasing sample thickness, and become zero in the bulk material. The 1T symmetry, which is different from the 2H symmetry in the MoS_2, would cause random stacking of $ReSe_2$, resulting in weaker interlayer modes in thicker samples and no observable interlayer modes in the bulk. This random stacking would decrease the intensities of interlayer with increasing layer number, because more layers will result in an increasing level of disorder.

Figure 2(c) shows the polarization dependence of the C and LB modes measured in bilayer and trilayer $ReSe_2$. Owing to the reduced in-plane symmetry in the $ReSe_2$ lattice, the intensity of the C and LB modes show strong dependence on the polarization angle of the incident laser beam. This clearly reveals the interlayer coupling characteristics and the anisotropic interlayer vibration modes in $ReSe_2$, which suggests that the ultralow frequency interlayer Raman measurements help estimate the layer number in $ReSe_2$ samples and their crystal orientation by Raman tensor analysis (see ESM).

The intralayer Raman modes of layered materials correspond to the Raman-active intralayer phonon vibration. The layer-number dependence of these high frequency Raman modes (> 50 cm^{-1}) can also provide insight into the interlayer interaction in 2D materials. In the high frequency region of the monolayer $ReSe_2$ Raman spectra, there should be 36 normal vibration modes including 18 potential Raman modes owing to the presence of 12 atoms in each unit cell of the $ReSe_2$ crystal lattice. We detected more than 10 distinctive Raman peaks in the spectral range between 100 and 300 cm^{-1} in the Raman spectrum of monolayer $ReSe_2$, as depicted in Fig. 3(a).

Owing to the reduced in-plane symmetry, the intensity of the intralayer Raman modes in $ReSe_2$ also exhibits strong polarization dependence. By varying the polarization direction of the incident laser beam, we investigated the polarization dependence of various Raman modes of monolayer $ReSe_2$. Measurements were carried out from 0° to 360° with 20° steps. Figure 3(a) shows a plot of Raman spectra under different polarization directions. There are no obvious shifts in the peak positions when tuning the polarization direction of the incident laser beam. However, the peak intensity of all the Raman modes varies significantly, with a period of 180°. This dependence can be clearly observed in the polar plots of the peak intensity as a function of the polarization angle. Figure 3(b) shows the plots for the peaks at 125, 160, and 176 cm^{-1}. Similar

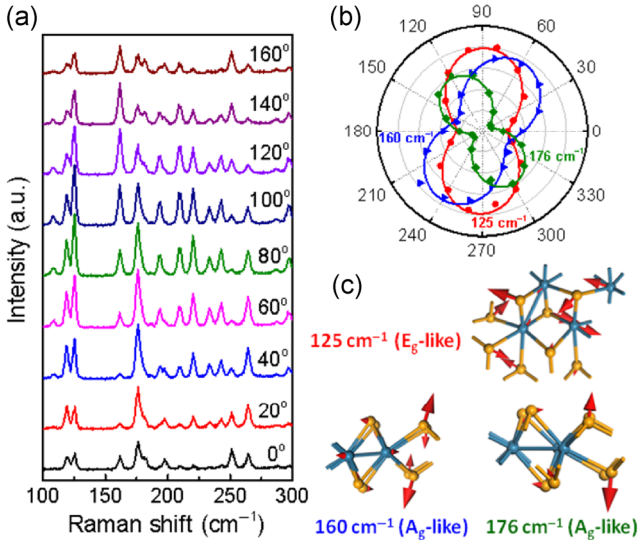

Figure 3 (a) Raman spectra of monolayer $ReSe_2$ in the 100 to 300 cm^{-1} spectral range under the excitation of a 532 nm green laser beam at different polarization directions incident normal to the sample. (b) The dependence of Raman intensity on the polarization of the incident laser beam for three typical peaks located at 125 cm^{-1} (red dots), 160 cm^{-1} (blue triangles), and 176 cm^{-1} (green diamonds). The symbols represent experimental data while the three curves in corresponding colors are fits from the Raman tensor analysis. (c) The lattice vibration modes of the three peaks shown in (b) obtained from first-principle calculations.

plots of additional characteristic peaks are available in Fig. S2 in the ESM. Since modifying the relative angle between the laser polarization direction and crystal orientation leads to variation in the Raman intensities, we can utilize the polarization-resolved Raman measurement as a non-destructive tool to identify the crystal orientation of $ReSe_2$. This is the first systematic study of high frequency Raman spectra in monolayer and bilayer $ReSe_2$. Our results are also consistent with a previous study [43] that showed Raman measurement data for five-layer and thicker $ReSe_2$ samples.

To understand the corresponding lattice vibrations of each Raman mode, we calculated the phonon modes of monolayer $ReSe_2$. Among the 36 normal modes of phonon vibrations, there are 18 Raman modes, 15 infrared modes, and three acoustic modes. Hence, the lattice vibration in each Raman mode can be rather complex. The vibrations of each Raman mode were identified by DFT. The calculated modes match well with the measured peaks. A table (Table S2 in the ESM) comparing the calculated and experimental peaks are provided. We found that the vibration in each mode contains multiple components along different lattice directions. In addition, since there are four Se basis atoms and two Re basis atoms in each unit cell, the intensity of vibration could vary significantly in atoms with different positions. Figure 3(c) shows the lattice vibration and atom displacement directions for the phonon modes corresponding to the 125, 160, and 176 cm^{-1} peaks. Owing to the complexity of lattice vibrations in monolayer $ReSe_2$, it is hard to find a pure E_g or A_g mode corresponding to each Raman peak, as is the case for MoS_2. Thus, we identify these modes as E_g-like or A_g-like modes based on their dominant vibration directions. The 125 cm^{-1} mode is an E_g-like mode, as the vibration is mostly in-plane and symmetric. The 160 and 176 cm^{-1} peaks are A_g-like modes since the main vibrations are in the one-dimensional vertical direction.

Figure 4 shows the layer-number dependence of the $ReSe_2$ Raman spectra for monolayer, bilayer, and four-layer samples. Bulk $ReSe_2$ displayed very weak Raman intensity, compared to its few-layer counterparts. For all of the peaks, except the one near 176 cm^{-1}, Raman intensities of monolayer samples are slightly weaker than those in the three-layer to four-layer samples. This is attributed to the small volume in the unit cell of the monolayer sample and the multiple reflection interference in the multilayer structures contained in the $ReSe_2$ flake, SiO_2, and Si substrate, similar to the case of graphene multilayers [44]. For most of the Raman modes, thick samples have red-shifted

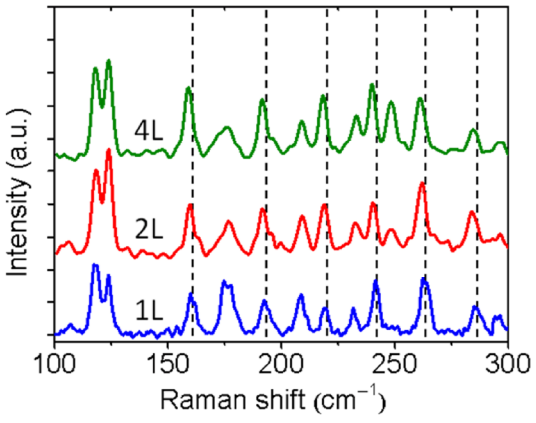

Figure 4 Layer-dependent Raman spectra of $ReSe_2$ in the 100 to 300 cm^{-1} range. The monolayer, bilayer, and four-layer flakes with the same crystal orientation were measured with the same polarization of the incident laser beam.

peak positions compared to the thinner samples. A detailed discussion of the layer-number dependence of high frequency Raman modes is included in the Discussions section.

Owing to interlayer coupling and 2D quantum confinement, the bandgap of atomically thin $ReSe_2$ samples depends on their layer number, as shown by PL measurements. We carried out PL measurements on monolayer, few-layer, and bulk $ReSe_2$ samples (Fig. 5(a)). For each sample, only one main PL peak was found. However, the PL spectrum of bulk $ReSe_2$ has a relatively broader peak, which is likely the combination of two split peaks. A detailed discussion of the PL split at low temperature can be found in the supplementary information. Owing to the indirect bandgap nature, the peak intensity is relatively weak for monolayer $ReSe_2$, and increases monotonically when adding layer numbers (Fig. 5(b)). Thus, the PL spectra of monolayer samples are relatively noisier than those of the few-layer samples. The measured bandgap enlarges with deceasing layer numbers, ranging from 1.26 eV for the bulk material to 1.32 eV for the monolayer crystals (Figs. 5(a) and 5(b)). The same trend in the layer-number dependence of the bandgap was predicted by previous first-principle calculations of $ReSe_2$ bandgap at different thicknesses [23].

To further study the anisotropic optical absorption, we conducted polarization-dependent PL measurements on few-layer $ReSe_2$ flakes by rotating the polarization of the incident laser beam. Since the PL signal of very thin $ReSe_2$ is relatively weak owing to its indirect bandgap, we chose multilayer samples to obtain a higher signal-to-noise ratio. Multilayer $ReSe_2$ regions of different thickness (six-layer and ten-layer) were selected from a single continuous flake sample, and thus should have the same crystal orientations, which is confirmed by Raman measurements. By varying the polarization direction of the excitation laser beam, we were able to obtain polarization-dependent PL peak intensities. As shown in Fig. 5(c), the peak intensity of two flake regions with six-layer and ten-layer $ReSe_2$ vary with polarization angles at a period of 180°, revealing their anisotropic energy-band information.

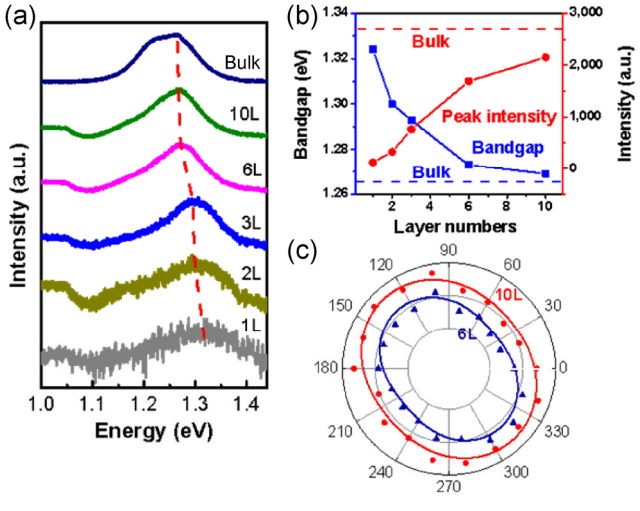

Figure 5 (a) PL spectrum of $ReSe_2$ in different layers. (b) The layer-dependent PL intensity and bandgap of few-layer $ReSe_2$. (c) Polarization-dependent PL intensity of six-layer and ten-layer $ReSe_2$.

3 Discussion

3.1 Ultralow-frequency interlayer Raman modes

Our ultralow frequency Raman measurement is the first experimental study of interlayer vibrations in few-layer $ReSe_2$. These interlayer Raman modes are important since they offer information about interlayer charge exchanges, screenings, and scatterings. The frequency of the observable C and LB modes of multilayer materials can be calculated by these two linear chain models (LCMs) [37], respectively

$$\omega(\mathrm{C}_{NN-i}) = \sqrt{2}\omega(\mathrm{C}_{21})\sin(i\pi/2N)$$

$$\omega(\mathrm{LB}_{NN-i}) = \sqrt{2}\omega(\mathrm{LB}_{21})\sin(i\pi/2N)$$

where N is the layer number, $i = 1, 2, \cdots, N-1$. By using this formula, the layer number can be determined from the peak positions of the C and LB modes. Compared to AFM data, measurements of ultralow frequency Raman modes provide a more accurate method for identifying $ReSe_2$ layer numbers. Our first-principle calculations were able to accurately predict the C and LB Raman modes of bilayer and trilayer $ReSe_2$. Additional information about the DFT-calculated (bilayer and trilayer) and LCM-fitting (bilayer, trilayer, six-layer, and ten-layer) modes can be found in Table S1 in the ESM. Owing to random stacking in the multilayer $ReSe_2$, the symmetry reduces from C_i (monolayer) to C_1

(multilayer). In a C_1 symmetry crystal, all Raman modes, including the low-frequency modes, are Raman active.

3.2 High frequency intralayer Raman modes

The high frequency Raman spectra of $ReSe_2$ corresponding to the intralayer modes are distinctively different from that in other typical TMDCs such as MoS_2 and WSe_2. Here, we compare the Raman spectra of few-layer $ReSe_2$ with those of few-layer MoS_2. Atomically thin $ReSe_2$ layers have more than ten measured Raman peaks while MoS_2 flakes only have two high frequency Raman active peaks [45], which are attributed to the E^1_{2g} mode and A_{1g} mode. In addition, the lattice vibrations in each $ReSe_2$ Raman mode are much more complex than those in MoS_2 layers. It can be easily identified that the E^1_{2g} mode of MoS_2 is the in-plane opposite vibration of two S atoms and one Mo atom, while the A_{1g} mode is the opposite vibration of two S atoms in the vertical direction. For $ReSe_2$, however, it is hard to identify such a pure vibration mode owing to the rather complicated crystal lattice, and hence, the Raman modes are named based on the dominant direction of phonon vibrations, for example, the E_g-like and A_g-like modes at 125, 160, and 176 cm^{-1}, as shown in Fig. 3(c).

Monolayer $ReSe_2$ has a C_i symmetry, and the corresponding irreducible representation is $\Gamma = A' + A''$, in which A′ is Raman active. Therefore, all Raman modes in $ReSe_2$ are the A′ mode with the same format of the Raman tensor

$$A' = \begin{bmatrix} a & d & e \\ d & b & f \\ e & f & c \end{bmatrix}$$

According to this tensor, the angle-resolved peak intensity of the Raman mode in the polarization measurement is calculated. If the polarization angle in the plane of incident laser is assumed to be φ, the intensity of the A′ mode is $I(A')\alpha|a\cos\varphi + d\sin\varphi|^2 + |d\cos\varphi + b\sin\varphi|^2$, resulting in the polarization-dependent nature of the intensity of the Raman modes. Using this concept, we are able to determine the crystal orientation of our samples by analyzing three of the characteristic Raman peaks; see ESM for details. The Raman tensor for each peak of monolayer $ReSe_2$ is different, which may lead to different angle-resolved polarization intensity profiles between two peaks. As shown in Fig. 3(b), our calculations fit the experimental results well.

It is also observed that most of the peak positions for monolayer and few-layer $ReSe_2$ samples red-shift with increasing layer numbers (Fig. 4). Considering vdW forces only, when the layer number increases, the vdW interaction between layers tends to suppress lattice vibrations, making the lattice more "stiff". Thus, the vibration energy of each vibration mode could increase with layer number, resulting in blue-shifts of the corresponding Raman peaks [42]. Conversely, if we consider long-range Coulomb interactions, the increase in dielectric tensors with the layer numbers can lead to an increase in Coulomb screenings. This results in a softer Coulomb interaction between atoms, and thus, the Raman peak tends to red-shift [46]. Here, we would like to compare $ReSe_2$ with WSe_2, whose atomic mass is almost equal to $ReSe_2$. The layer-number-dependent behavior of high frequency modes in WSe_2 is similar with that in MoS_2: The A_{1g} and E_{2g} modes blue-shift and red-shift from monolayer to bulk, respectively [47]. The frequencies of the C and LB modes in bilayer WSe_2 are 16.5 and 28.2 cm^{-1}, respectively [38], which are higher than those in bilayer $ReSe_2$. The vdW interaction can be measured by the interlayer force constant $a\alpha m\omega^2$ [36], where m is atomic mass of monolayer TMDCs, ω is the Raman frequency of the interlayer vibration modes. Since m is almost the same for each layer, the interlayer C and LB coupling of WSe_2 are about 27% and 49% stronger than that of $ReSe_2$, respectively. This indicates that the interlayer vdW interaction of $ReSe_2$ is much weaker than that of WSe_2. Moreover, the long range Coulomb interaction is estimated from DFT calculations of the dielectric tensors and Born effective charges (see ESM). The long range Coulomb interaction in $ReSe_2$ is similar to that of WSe_2. Based on the above discussions, the observed red-shifts of Raman peaks with increasing $ReSe_2$ layer numbers indicate that the interlayer vdW interaction is not strong enough to dominate the layer dependence of phonon behavior. The relative weak interlayer coupling of few-layer $ReSe_2$ has also been evidenced by its layer-number-dependent PL emission, which will be discussed later.

For both ultralow frequency and high frequency in-plane Raman modes, the peak intensities vary periodically with the polarization directions of the incident laser beam, which is direct evidence of the anisotropy crystal. By combining high frequency and low frequency Raman measurements, both crystal orientation and layer numbers of $ReSe_2$ flakes can be clearly identified.

3.3 Photoluminescence

For layered materials, the quantum confinement in the vertical direction can be enhanced once the layer number reduces and the interlayer interaction disappears in monolayer samples. Hence, many TMDC crystals have indirect energy bandgap in their bulk and multilayer forms, but possess direct bandgap in their monolayer form [45, 48, 49]. The photoluminescence measurements of monolayer and few-layer $ReSe_2$ samples revealed that the optical bandgap decreases with increasing layer numbers (Fig. 5(b)), which is similar to other 2D semiconductors, such as MoS_2 [50], black phosphorus [51], and ReS_2 [24]. As is the case with ReS_2, the layer-number-dependence of the bandgap of few-layer $ReSe_2$ is much weaker than that in other 2D semiconductors. Many TMDCs such as MoS_2 and WSe_2 have strong PL emission in monolayer flakes with direct bandgap; however, the PL peak intensity of few-layer $ReSe_2$ increases monotonically when increasing the layer number (Fig. 5(b)). The layer-number dependence of the PL peak intensity is much weaker compared to other TMDCs such as MoS_2 and WSe_2, indicating a relatively weak layer-number dependence of quantum confinement and interlayer interactions. In this case, PL intensity increases with layer number owing to the increased quantity of the material.

In summary, we report the first experimental observation of the anisotropic interlayer C and LB vibration modes and the anisotropic layer-number-dependent photoluminescence in monolayer and few-layer $ReSe_2$. A systematic study of the angle-resolved polarization Raman measurements on intralayer Raman modes of monolayer and bilayer $ReSe_2$, as well as their layer-number dependence, is also carried out for the first time. The ultralow frequency Raman modes can be used for the identification of the layer number and crystal orientation in $ReSe_2$. The optical bandgaps of $ReSe_2$ are revealed to vary from 1.32 eV in the monolayer to 1.26 eV in the bulk, which agree well with the first-principle calculations. Information on the interlayer Raman modes and the layer-number-dependent optical bandgap in $ReSe_2$ advances the understanding of this 2D TMDC material with an unusually complex lattice structure while opening the door to potential applications in near-infrared polarized optoelectronics devices. Finally, the experimental demonstration of anisotropic phonon and optical properties also provides direct experimental evidence of the highly anisotropic nature of monolayer and few-layer $ReSe_2$, which may be utilized to construct advanced semiconductor devices. Furthermore, apart from tuning the $ReSe_2$ bandgap via modifying the layer numbers, strain engineering [29] and electrostatic gating [52] could also be utilized to control the energy bandgap. Since the indirect bandgap of $ReSe_2$ is just slightly smaller than the direct inter-band transition energy, as shown in the electronic band structure, it might be possible to tune $ReSe_2$ into a direct bandgap material with bandgap engineering, which is desirable for various applications like light emission. Owing to its tunable bandgap in the NIR spectrum, $ReSe_2$ is an interesting material for exploring novel device applications in NIR optoelectonics.

4 Methods

4.1 Sample preparation and imaging

$ReSe_2$ flakes were exfoliated from bulk $ReSe_2$ crystals onto high resistivity silicon substrates with 285-nm-thick SiO_2 using the standard micromechanical exfoliation method. An optical microscope was used to locate few-layer samples via optical contrast. Then, the layer numbers were carefully identified by a Dimension Edge AFM.

4.2 High frequency interlayer Raman measurements

High frequency Raman spectroscopy was measured by a Renishaw InVia spectrometer with 532 nm green laser. In typical measurements, 0.2 mW laser power was applied for 60 s through an X100 objective. A half-wavelength plate was used to tune the polarization of the incident laser beam. All Raman measurements

were conducted in a dark environment at room temperature.

4.3 Ultralow frequency intralayer Raman measurements

The Raman spectra at ultralow frequencies were measured in the back-scattering mode at room temperature with a Jobin–Yvon HR800 Raman system, equipped with a liquid-nitrogen-cooled CCD, an X100 objective lens (numerical aperture: 0.90), and 1800 lines/mm gratings. The excitation wavelength was 530 nm from a Kr^+ laser. Plasma lines were removed from the laser signals using BragGrate band-pass filters. Measurements down to 5 cm^{-1} for each excitation were enabled by three BragGrate notch filters with an optical density of 3 and a full width at half maximum (FWHM) in the range 5–10 cm^{-1}. The BragGrate band-pass and notch filters are produced by OptiGrate Corp.

4.4 Photoluminescence measurements

Photoluminescence was measured with a Jobin–Yvon HR800 Raman system, equipped with a liquid-nitrogen-cooled InGaAs detector, an X50 objective lens (numerical aperture: 0.55), and 150 lines/mm gratings. The excitation wavelength was 633 nm from a He–Ne laser. A ST500 system was employed to cool the samples to 80 K.

4.5 First-principle calculations

For the calculation of $ReSe_2$ bandstructure, various methods were used, and consistent results were obtained. Ultrasoft pseudo-potential was applied, which has been proven to work well for 2D materials. All energy bandstructure diagrams plotted in this paper were generated by the Perdew–Burke–Ernzerhof exchange-correlation function under general gradient approximations, as implanted in the framework of DFT and as implemented in the Vienna *ab initio* simulation package (VASP). The K-space paths were selected to pass through most of the highly symmetric points in the reciprocal space, as shown in Fig. 1(b). Non-collinear spin polarization was considered for SOC related calculations. We found that the neglect of SOC or spin polarization always results in a higher bandgap, although GGA itself typically underestimates the bandgap for 2D materials. The projector augmented wave (PAW) method and a plane-wave basis set with an energy cutoff of 500 eV were used in the calculations. For geometry optimizations, the Brillouin-zone integration was performed using a regular 5 × 5 × 5 and 5 × 5 × 1 k mesh within the Monkhorst–Pack scheme for bulk and monolayer samples, respectively. The k-points have been doubled for the electronic density of states calculations. The convergence criterion of the self-consistent field calculations was set to 10^{-5} eV for the total energy. The lattice constants were optimized until the atomic forces are less than 0.01 eV/Å. For monolayer samples, a large vacuum spacing (at least 12 Å) was introduced.

Lattice vibrations for monolayer, bilayer, and trilayer $ReSe_2$ were also calculated using the GGA–PBE scheme with the K-path shown in Fig. 1(b). K-point sampling was 8 × 8 × 1 for monolayer sample, and 4 × 4 × 1 for the bilayer and trilayer ones. Before all calculations carried out in this study, the geometry of the crystal structures was optimized.

Acknowledgements

This work is partially supported by National Science Foundation EFRI 2-DARE program (No. 1542815) and Zumberge Research and Innovation Fund Award. P.-H. Tan acknowledges support from the National Natural Science Foundation of China (Nos. 11225421, 11474277, and 11434010).

Electronic Supplementary Material: Supplementary material (more experimental data, theoretical explanation, and DFT calculation of $ReSe_2$ Raman and PL) is available in the online version of this article at http://dx.doi.org/10.1007/s12274-015-0865-0.

References

[1] Wang, Q. H.; Kalantar-Zadeh, K.; Kis, A.; Coleman, J. N.; Strano, M. S. Electronics and optoelectronics of two-dimensional transition metal dichalcogenides. *Nat. Nanotechnol.* **2012**, *7*, 699–712.

[2] Geim, A. K.; Grigorieva, I. V. Van der Waals heterostructures. *Nature* **2013**, *499*, 419–425.

[3] Chhowalla, M.; Shin, H. S.; Eda, G.; Li, L.-J.; Loh, K. P.; Zhang, H. The chemistry of two-dimensional layered transition metal dichalcogenide nanosheets. *Nat. Chem.* **2013**, *5*, 263–275.

[4] Xu, X. D.; Yao, W.; Xiao, D.; Heinz, T. F. Spin and pseudospins in layered transition metal dichalcogenides. *Nat. Phys.* **2014**, *10*, 343–350.

[5] Lee, Y.-H.; Yu, L. L.; Wang, H.; Fang, W. J.; Ling, X.; Shi, Y. M.; Lin, C.-T.; Huang, J.-K.; Chang, M.-T.; Chang, C.-S. et al. Synthesis and transfer of single-layer transition metal disulfides on diverse surfaces. *Nano Lett.* **2013**, *13*, 1852–1857.

[6] Rice, C.; Young, R. J.; Zan, R.; Bangert, U.; Wolverson, D.; Georgiou, T.; Jalil, R.; Novoselov, K. S. Raman-scattering measurements and first-principles calculations of strain-induced phonon shifts in monolayer MoS_2. *Phys. Rev. B* **2013**, *87*, 081307.

[7] Ling, X.; Wang, H.; Huang, S. X.; Xia, F. N.; Dresselhaus, M. S. The renaissance of black phosphorus. *Proc. Natl. Acad. Sci. USA* **2015**, *112*, 4523–4530.

[8] Li, L. K.; Yu, Y. J.; Ye, G. J.; Ge, Q. Q.; Ou, X. D.; Wu, H.; Feng, D. L.; Chen, X. H.; Zhang, Y. B. Black phosphorus field-effect transistors. *Nat. Nanotechnol.* **2014**, *9*, 372–377.

[9] Xia, F. N.; Wang, H.; Jia, Y. C. Rediscovering black phosphorus as an anisotropic layered material for optoelectronics and electronics. *Nat. Commun.* **2014**, *5*, 4458.

[10] Liu, H.; Neal, A. T.; Zhu, Z.; Luo, Z.; Xu, X. F.; Tománek, D.; Ye, P. D. Phosphorene: An unexplored 2D semiconductor with a high hole mobility. *ACS Nano* **2014**, *8*, 4033–4041.

[11] Avsar, A.; Vera-Marun, I. J.; Tan, J. Y.; Watanabe, K.; Taniguchi, T.; Castro Neto, A. H.; Özyilmaz, B. Air-stable transport in graphene-contacted, fully encapsulated ultrathin black phosphorus-based field-effect transistors. *ACS Nano* **2015**, *9*, 4138–4145.

[12] Wang, H.; Wang, X. M.; Xia, F. N.; Wang, L. H.; Jiang, H.; Xia, Q. F.; Chin, M. L.; Dubey, M.; Han, S.-J. Black phosphorus radio-frequency transistors. *Nano Lett.* **2014**, *14*, 6424–6429.

[13] Haratipour, N.; Robbins, M. C.; Koester, S. J. Black phosphorus p-MOSFETs with 7-nm HfO_2 gate dielectric and low contact resistance. *IEEE Electr. Device Lett.* **2015**, *36*, 411–413.

[14] Youngblood, N.; Chen, C.; Koester, S. J.; Li, M. Waveguide-integrated black phosphorus photodetector with high responsivity and low dark current. *Nat. Photon.* **2015**, *9*, 247–252.

[15] Buscema, M.; Groenendijk, D. J.; Blanter, S. I.; Steele, G. A.; van der Zant, H. S. J.; Castellanos-Gomez, A. Fast and broadband photoresponse of few-layer black phosphorus field-effect transistors. *Nano Lett.* **2014**, *14*, 3347–3352.

[16] Low, T.; Rodin, A. S.; Carvalho, A.; Jiang, Y. J.; Wang, H.; Xia, F. N.; Neto, A. H. C. Tunable optical properties of multilayer black phosphorus thin films. *Phys. Rev. B* **2014**, *90*, 075434.

[17] Xia, F. N.; Wang, H.; Xiao, D.; Dubey, M.; Ramasubramaniam, A. Two-dimensional material nanophotonics. *Nat. Photon.* **2014**, *8*, 899–907.

[18] Zhao, H.; Guo, Q. S.; Xia, F. N.; Wang, H. Two-dimensional materials for nanophotonics application. *Nanophotonics*, in press, DOI: 10.1515/nanoph-2014-0022.

[19] Fei, R. X.; Faghaninia, A.; Soklaski, R.; Yan, J.-A.; Lo, C.; Yang, L. Enhanced thermoelectric efficiency via orthogonal electrical and thermal conductances in phosphorene. *Nano Lett.* **2014**, *14*, 6393–6399.

[20] Lamfers, H.-J.; Meetsma, A.; Wiegers, G.; De Boer, J. The crystal structure of some rhenium and technetium dichalcogenides. *J. Alloy. Compd.* **1996**, *241*, 34–39.

[21] Kertesz, M.; Hoffmann, R. Octahedral vs. trigonal-prismatic coordination and clustering in transition-metal dichalcogenides. *J. Am. Chem. Soc.* **1984**, *106*, 3453–3460.

[22] Fang, C. M.; Wiegers, G. A.; Haas, C.; De Groot, R. A. Electronic structures of ReS_2, ReS_2 and TcS_2 in the real and the hypothetical undistorted structures. *J. Phys.: Condens. Matter* **1997**, *9*, 4411–4424.

[23] Yang, S. X.; Tongay, S.; Li, Y.; Yue, Q.; Xia, J.-B.; Li, S.-S.; Li, J. B.; Wei, S.-H. Layer-dependent electrical and optoelectronic responses of $ReSe_2$ nanosheet transistors. *Nanoscale* **2014**, *6*, 7226–7231.

[24] Tongay, S.; Sahin, H.; Ko, C.; Luce, A.; Fan, W.; Liu, K.; Zhou, J.; Huang, Y.-S.; Ho, C.-H.; Yan, J. Y. et al. Monolayer behaviour in bulk ReS_2 due to electronic and vibrational decoupling. *Nat. Commun.* **2014**, *5*, 3252.

[25] Friemelt, K.; Lux-Steiner, M. C.; Bucher, E. Optical properties of the layered transition-metal-dichalcogenide ReS_2: Anisotropy in the van der Waals plane. *J. Appl. Phys.* **1993**, *74*, 5266–5268.

[26] Ho, C. H.; Huang, Y. S.; Tiong, K. K.; Liao, P. C. Absorption-edge anisotropy in ReS_2 and $ReSe_2$ layered semiconductors. *Phys. Rev. B* **1998**, *58*, 16130–16135.

[27] Ho, C. H.; Huang, Y. S.; Tiong, K. K. In-plane anisotropy of the optical and electrical properties of ReS_2 and $ReSe_2$ layered crystals. *J. Alloy. Compd.* **2001**, *317-318*, 222–226.

[28] Ho, C.-H. Dichroic electro-optical behavior of rhenium sulfide layered crystal. *Crystal Struct. Theory Appl.* **2013**, *2*, 65–69.

[29] Yang, S. X.; Wang, C.; Sahin, H.; Chen, H.; Li, Y.; Li, S.-S.; Suslu, A.; Peeters, F. M.; Liu, Q.; Li, J. B. et al. Tuning the optical, magnetic, and electrical properties of $ReSe_2$ by nanoscale strain engineering. *Nano Lett.* **2015**, *15*, 1660–1666.

[30] Jian, Y.-C.; Lin, D.-Y.; Wu, J.-S.; Huang, Y.-S. Optical and electrical properties of Au- and Ag-doped $ReSe_2$. *Jpn. J. Appl. Phys.* **2013**, *52*, 04CH06.

[31] Kao, Y.-C.; Huang, T.; Lin, D.-Y.; Huang, Y.-S.; Tiong, K.-K.; Lee, H.-Y.; Lin, J.-M.; Sheu, H.-S.; Lin, C.-M. Anomalous structural phase transition properties in $ReSe_2$ and Au-doped $ReSe_2$. *J. Chem. Phys.* **2012**, *137*, 024509.

[32] Yang, S. X.; Tongay, S.; Yue, Q.; Li, Y. T.; Li, B.; Lu, F. Y. High-performance few-layer Mo-doped $ReSe_2$ nanosheet photodetectors. *Sci. Rep.* **2014**, *4*, 5442.

[33] Pickett, W. E. Pseudopotential methods in condensed matter applications. *Comput. Phys. Rep.* **1989**, *9*, 115–197.

[34] Novoselov, K. S.; Geim, A. K.; Morozov, S.; Jiang, D.; Zhang, Y.; Dubonos, S.; Grigorieva, I.; Firsov, A. Electric field effect in atomically thin carbon films. *Science* **2004**, *306*, 666–669.

[35] Alcock, N. W.; Kjekshus, A. The crystal structure of $ReSe_2$. *Acta Chem. Scand.* **1965**, *19*, 79–94.

[36] Tan, P. H.; Han, W. P.; Zhao, W. J.; Wu, Z. H.; Chang, K.; Wang, H.; Wang, Y. F.; Bonini, N.; Marzari, N.; Pugno, N. et al. The shear mode of multilayer graphene. *Nat Mater* **2012**, *11*, 294–300.

[37] Zhang, X.; Han, W. P.; Wu, J. B.; Milana, S.; Lu, Y.; Li, Q. Q.; Ferrari, A. C.; Tan, P. H. Raman spectroscopy of shear and layer breathing modes in multilayer MoS_2. *Phys. Rev. B* **2013**, *87*, 115413.

[38] Zhao, Y. Y.; Luo, X.; Li, H.; Zhang, J.; Araujo, P. T.; Gan, C. K.; Wu, J.; Zhang, H.; Quek, S. Y.; Dresselhaus, M. S. et al. Interlayer breathing and shear modes in few-trilayer MoS_2 and WSe_2. *Nano Lett.* **2013**, *13*, 1007–1015.

[39] Tan, P.-H.; Wu, J.-B.; Han, W.-P.; Zhao, W.-J.; Zhang, X.; Wang, H.; Wang, Y.-F. Ultralow-frequency shear modes of 2-4 layer graphene observed in scroll structures at edges. *Phys. Rev. B* **2014**, *89*, 235404.

[40] Ling, X.; Liang, L. B.; Huang, S. X.; Puretzky, A. A.; Geohegan, D. B.; Sumpter, B. G.; Kong, J.; Meunier, V.; Dresselhaus, M. S. Observation of low-frequency interlayer breathing modes in few-layer black phosphorus. 2015, arXiv: materials science/1502.07804. arXiv.org e-Print archive. http://archiv.org/abs/1502.07804.

[41] Wu, J.-B.; Zhang, X.; Ijäs, M.; Han, W.-P.; Qiao, X.-F.; Li, X.-L.; Jiang, D.-S.; Ferrari, A. C.; Tan, P.-H. Resonant Raman spectroscopy of twisted multilayer graphene. *Nat. Commun.* **2014**, *5*, 5309.

[42] Zhang, X.; Qiao, X.-F.; Shi, W.; Wu, J.-B.; Jiang, D.-S.; Tan, P.-H. Phonon and Raman scattering of two-dimensional transition metal dichalcogenides from monolayer, multilayer to bulk material. *Chem. Soc. Rev.* **2015**, *44*, 2757–2785.

[43] Wolverson, D.; Crampin, S.; Kazemi, A. S.; Ilie, A.; Bending, S. J. Raman spectra of monolayer, few-layer, and bulk $ReSe_2$: An anisotropic layered semiconductor. *ACS Nano* **2014**, *8*, 11154–11164.

[44] Li, X. L.; Qiao, X. F.; Han, W.-P.; Lu, Y.; Tan, Q.-H.; Liu, X.-L.; Tan, P. H. Layer number identification of intrinsic and defective multilayered graphenes up to 100 layers by the Raman mode intensity from substrates . *Nanoscale* **2015**, *7*, 8135–8141.

[45] Li, H.; Zhang, Q.; Yap, C. C. R.; Tay, B. K.; Edwin, T. H. T.; Olivier, A.; Baillargeat, D. From bulk to monolayer MoS_2: Evolution of Raman scattering. *Adv. Funct. Mater.* **2012**, *22*, 1385–1390.

[46] Molina-Sánchez, A.; Wirtz, L. Phonons in single-layer and few-layer MoS_2 and WS_2. *Phys. Rev. B* **2011**, *84*, 155413.

[47] Zhao, W. J.; Ghorannevis, Z.; Amara, K. K.; Pang, J. R.; Toh, M.; Zhang, X.; Kloc, C.; Tan, P. H.; Eda, G. Lattice dynamics in mono- and few-layer sheets of WS_2 and WSe_2. *Nanoscale* **2013**, *5*, 9677–9683.

[48] Tongay, S.; Zhou, J.; Ataca, C.; Lo, K.; Matthews, T. S.; Li, J. B.; Grossman, J. C.; Wu, J. Q. Thermally driven crossover from indirect toward direct bandgap in 2D semiconductors: $MoSe_2$ versus MoS_2. *Nano Lett.* **2012**, *12*, 5576–5580.

[49] Zhao, W. J.; Ghorannevis, Z.; Chu, L. Q.; Toh, M.; Kloc, C.; Tan, P.-H.; Eda, G. Evolution of electronic structure in atomically thin sheets of WS_2 and WSe_2. *Acs Nano* **2012**, *7*, 791–797.

[50] Splendiani, A.; Sun, L.; Zhang, Y.; Li, T.; Kim, J.; Chim, C.-Y.; Galli, G.; Wang, F. Emerging photoluminescence in monolayer MoS_2. *Nano Lett.* **2010**, *10*, 1271–1275.

[51] Wang, X. M.; Jones, A. M.; Seyler, K. L.; Tran, V.; Jia, Y. C.; Zhao, H.; Wang, H.; Yang, L.; Xu, X. D.; Xia, F. N. Highly anisotropic and robust excitons in monolayer black phosphorus. 2014, arXiv: mesoscale and nanoscale physics/1411.1695. arXiv.org e-Print archive. http://archiv.org/abs/1411.1695.

[52] Li, Z.; Chang, S.-W.; Chen, C.-C.; Cronin, S. B. Enhanced photocurrent and photoluminescence spectra in MoS_2 under ionic liquid gating. *Nano Res.* **2014**, *7*, 973–980.